

RESONANCE STRUCTURE AND POLARIZABILITY OF THE NUCLEON

D. DRECHSEL

*Institut für Kernphysik, Johannes Gutenberg-Universität,
Becherweg 45,
55099 Mainz, Germany
E-mail: drechsel@kph.uni-mainz.de*

The main features of the resonance structure of the nucleon are discussed, particular with regard to the helicity dependence of real and virtual photoabsorption. The dependence of the partial cross sections on both the resonance helicity amplitudes and the electromagnetic multipoles is outlined. The general structure of the Compton tensor is reviewed and applied to the special cases of real to real, virtual to real, and virtual to virtual Compton scattering. Recent theoretical developments in dispersion relations are presented, together with a short overview regarding static, dynamical, and generalized polarizabilities of the nucleon as well as the status of the Gerasimov-Drell-Hearn sum rule and related integrals.

1. The Resonance Structure of the Nucleon

On top of a nonresonant background, the total photoabsorption cross section of the nucleon exhibits three resonance regions, mainly corresponding to the resonances $\Delta(1232)$, $N^*(1520)$, and $N^*(1680)$ with dominance of magnetic dipole (M1), electric dipole (E1), and electric quadrupole (E2) radiation, respectively ¹. Above the third resonance region, the absorption cross section levels off at a value of about $120 \mu b$. At the highest measured energies, at total *c.m.* energy $W \simeq 200$ GeV, the cross section increases slowly ², in accordance with the soft pomeron exchange mechanism.

The resonance structures stick out much more clearly in the recent double-polarization experiments performed at MAMI ³ and ELSA ⁴. In these investigations, circularly polarized photons are absorbed by protons with polarization parallel and antiparallel to the photon momentum, which leads to hadronic excitations with helicities $3/2$ and $1/2$, respectively, as described in Fig. 1. The difference of the two helicity cross sections, $\sigma_{3/2} - \sigma_{1/2}$, displays the following features as function of the photon *lab* energy E_γ : (I) Negative values near threshold due to S-wave pion production, (II) a large (positive) peak at the position of the $\Delta(1232)$, (III) another

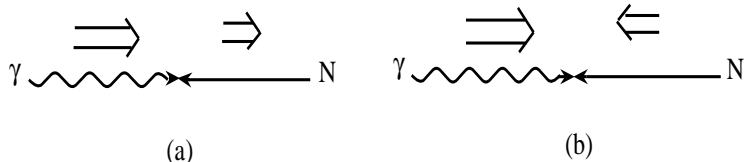


Figure 1. Spin and helicity of a double polarization experiment. The arrows \Rightarrow denote the spin projections on the photon momentum, the arrows \rightarrow the momenta of the particles. The spin projection and helicity of the photon is assumed to be $h_\gamma = 1$. The spin projection and helicity of the target nucleon N are denoted by S_z and h , respectively, and the eigenvalues of the excited system N^* by the corresponding primed quantities.

a) Helicity 3/2: Transition $N^*(S_z = 1/2, h_N = -1/2) \rightarrow N^*(S_z = h_{N^*} = 3/2)$, which changes the helicity by 2 units.

b) Helicity 1/2: Transition $N(S_z = -1/2, h_N = +1/2) \rightarrow (S_z = h_{N^*} = +1/2)$, which conserves the helicity.

peak somewhat below the $N^*(1520)$, mostly due to the onset of two-pion production, (IV) a somewhat smaller peak in the third resonance region, and (V) very small helicity differences at the higher energies, with a possible cross-over to negative values above $E_\gamma \approx 2$ GeV. In other words, the large background showing in the total cross section is “helicity blind” and drops out in measurements of the helicity difference.

By use of inelastic electron scattering the absorption cross section may be generalized to virtual photons characterized by energy transfer ν and four-momentum squared, Q^2 , and expressed in terms of a virtual photon flux factor Γ_V and four partial cross sections ⁵,

$$\frac{d\sigma}{d\Omega dE'} = \Gamma_V \sigma(\nu, Q^2), \quad (1)$$

$$\sigma = \sigma_T + \epsilon \sigma_L - hP_x \sqrt{2\epsilon(1-\epsilon)} \sigma_{LT} - hP_z \sqrt{1-\epsilon^2} \sigma_{TT}, \quad (2)$$

with the photon polarization ϵ . The four partial cross sections σ_T , σ_L , σ_{TT} and σ_{LT} are uniquely determined by the quark structure functions, F_1 , F_2 , g_1 and g_2 . Furthermore, the transverse cross sections are related to the partial cross sections $\sigma_{3/2}$ and $\sigma_{1/2}$ of Fig. 1(a) and 1(b), respectively, $\sigma_T = (\sigma_{1/2} + \sigma_{3/2})/2$, $\sigma_{TT} = (\sigma_{1/2} - \sigma_{3/2})/2$.

While the partial cross sections are usually considered as functions of ν and Q^2 , the quark structure functions are written as functions of x and Q^2 , where $x = Q^2/2m\nu$ is the Björken scaling variable. In the region of deep inelastic scattering (DIS), where the masses of the constituents can

be neglected, the observables should only depend on the specific ratio given by Björken's definition.

On the hadronic side the resonances can be described by either their helicity amplitudes or the multipoles of the pion-nucleon system in the final state. The helicity h of a particle is given by the projection of its spin \vec{s} onto the direction of its momentum, \hat{k} . Since the projection of orbital momentum onto this axis vanishes, only the intrinsic spin is involved, and consequently the nucleon takes the values $h_N = \pm\frac{1}{2}$, while the virtual photon has $h_\gamma = \pm 1$ and 0. The helicity is a pseudoscalar, invariant under rotations but changing sign under the parity transformation. If the hadronic states have good parity, only 3 of the 6 helicity amplitudes are independent: the two transverse amplitudes corresponding to Fig. 1,

$A_{3/2}(h_N = -\frac{1}{2}, h_\gamma = 1 \rightarrow h_{N^*} = \frac{3}{2})$, $A_{1/2}(h_N = \frac{1}{2}, h_\gamma = 1 \rightarrow h_{N^*} = \frac{1}{2})$, and the longitudinal amplitude $S_{1/2}(h_N = -\frac{1}{2}, h_\gamma = 0 \rightarrow h_{N^*} = \frac{1}{2})$.

In the case of an isolated resonance, the partial cross sections are related to the helicity amplitudes as follows:

$$\sigma_{1/2} \sim |A_{1/2}|^2, \quad \sigma_{3/2} \sim |A_{3/2}|^2, \quad \sigma_L \sim |S_{1/2}|^2, \quad \sigma_{LT} \sim S_{1/2}^* A_{1/2}. \quad (3)$$

The alternative description is in terms of electric (E), magnetic (M), and "scalar" (S) multipoles. These are further characterized by the relative orbital momentum l of the pion-nucleon final state and a sign, which is plus or minus if the total angular momentum J is equal to $l + \frac{1}{2}$ or $l - \frac{1}{2}$, respectively. The multipole content of the most important resonances is given in Table 1. As an example the P_{33} partial wave corresponds to the $\Delta(1232)$ with spin and isospin $3/2$, orbital momentum $l = 1$, and positive parity. Its multipoles are therefore M_{1+} (magnetic dipole radiation), E_{1+} (electric quadrupole), and S_{1+} (Coulomb quadrupole).

Table 1. The multipole contributions to the partial cross sections for some selected resonances. The entries have to be multiplied by overall kinematical factors.

resonance	σ_L	$\sigma_{3/2}$	$\sigma_{1/2}$	σ_{LT}
P_{33}	$8 S_{1+} ^2$	$3 E_{1+} - M_{1+} ^2$	$ 3E_{1+} + M_{1+} ^2$	$+2S_{1+}^*(3E_{1+} + M_{1+})$
P_{11}	$ S_{1-} ^2$	—	$2 M_{1-} ^2$	$-S_{1-}^* M_{1-}$
D_{13}	$8 S_{2-} ^2$	$3 E_{2-} + M_{2-} ^2$	$ E_{2-} - 3M_{2-} ^2$	$+2S_{2-}^*(E_{2-} - 3M_{2-})$
S_{11}	$ S_{0+} ^2$	—	$2 E_{0+} ^2$	$+S_{0+}^* E_{0+}$
D_{15}	$27 S_{2+} ^2$	$12 E_{2+} - M_{2+} ^2$	$6 2E_{2+} + M_{2+} ^2$	$+9S_{2+}^*(2E_{2+} + M_{2+})$
F_{15}	$27 S_{3-} ^2$	$12 E_{3-} + M_{3-} ^2$	$6 E_{3-} - 2M_{3-} ^2$	$+9S_{3-}^*(E_{3-} - 2M_{3-})$

The helicity structure of the resonance region changes with increasing "virtuality" Q^2 , as can be seen from Fig. 2 of Ref. ⁵. The main features are:
(I) The $\sigma_{1/2}$ contribution of pion threshold production decreases rapidly

with increasing Q^2 , (II) the $\sigma_{3/2}$ dominated $\Delta(1232)$ cross section remains nearly constant up to $Q^2 \approx 0.5 \text{ GeV}^2$ but drops strongly thereafter, (III) the helicity difference $\sigma_{3/2} - \sigma_{1/2}$ in the second and third resonance regions of the proton is positive for $Q^2 = 0$ but becomes negative already at $Q^2 \approx 0.5 \text{ GeV}^2$. This feature can be understood by strong electric multipoles E_{2-} and E_{3-} for real photons but an increase of the corresponding magnetic multipoles with virtuality Q^2 (see Table 1), such that the helicity amplitude $A_{3/2}$ dominates at $Q^2 = 0$ while $A_{1/2}$ takes over for large Q^2 , because it conserves the helicity.

2. Compton Scattering

By use of Lorentz and gauge invariance, crossing symmetry, parity and time reversal invariance, the amplitude for Compton scattering takes the form ⁶

$$\langle \chi_f | \mathcal{T} | \chi_i \rangle = \epsilon'_\mu \epsilon_\nu \sum_{\lambda=1}^{\lambda_{\max}} \langle \chi_f | \mathcal{O}_\lambda^{\mu\nu} | \chi_i \rangle \tilde{A}_\lambda(s, t), \quad (4)$$

where $\mathcal{O}_\lambda^{\mu\nu}$ are Lorentz tensors constructed from kinematical variables and γ matrices, and \tilde{A}_λ are Lorentz scalars. In the *c.m.* frame, these Lorentz structures can be reduced to Pauli matrices $\vec{\sigma}$ combined with unit vectors in the directions of the initial (\hat{k}) and final (\hat{k}') photons. The polarization vectors of the initial and final photons are denoted by $\vec{\epsilon}$ and $\vec{\epsilon}'$ for transverse polarization, and \hat{k} and \hat{k}' for longitudinal polarization. Special cases are:

I. Real Compton Scattering (RCS)

From helicity arguments there should be $2^4 = 16$ amplitudes, but parity conservation reduces this number to 8. In the *c.m.* frame the transition operator can be cast into the form

$$\begin{aligned} \mathcal{T}_{RR} = & A_1(\omega, \theta) \vec{\epsilon}' \cdot \vec{\epsilon} + A_2(\omega, \theta) \vec{\epsilon}' \cdot \hat{k} \vec{\epsilon} \cdot \hat{k}' \\ & + iA_3(\omega, \theta) \vec{\sigma} \cdot (\vec{\epsilon}' \times \vec{\epsilon}) + iA_4(\omega, \theta) \vec{\sigma} \cdot (\hat{k}' \times \hat{k}) \vec{\epsilon}' \cdot \vec{\epsilon} \\ & + iA_5(\omega, \theta) \vec{\sigma} \cdot \left[(\vec{\epsilon}' \times \hat{k}) \vec{\epsilon} \cdot \hat{k}' - (\vec{\epsilon} \times \hat{k}') \vec{\epsilon}' \cdot \hat{k} \right] \\ & + iA_6(\omega, \theta) \vec{\sigma} \cdot \left[(\vec{\epsilon}' \times \hat{k}') \vec{\epsilon} \cdot \hat{k}' - (\vec{\epsilon} \times \hat{k}) \vec{\epsilon}' \cdot \hat{k} \right] \\ & + iA_7(\omega, \theta) \vec{\sigma} \cdot \left[(\vec{\epsilon}' \times \hat{k}) \vec{\epsilon} \cdot \hat{k}' + (\vec{\epsilon} \times \hat{k}') \vec{\epsilon}' \cdot \hat{k} \right] \\ & + iA_8(\omega, \theta) \vec{\sigma} \cdot \left[(\vec{\epsilon}' \times \hat{k}') \vec{\epsilon} \cdot \hat{k}' + (\vec{\epsilon} \times \hat{k}) \vec{\epsilon}' \cdot \hat{k} \right], \quad (5) \end{aligned}$$

where ω is the energy and θ the scattering angle of the photon in the *c.m.* system.

By use of time reversal ($\hat{k} \leftrightarrow -\hat{k}'$, $\vec{\epsilon} \leftrightarrow \vec{\epsilon}'^*$, $i\vec{\sigma} \rightarrow -i\vec{\sigma}$) A_7 and A_8 change sign, and therefore vanish if time reversal invariance holds. Hence the transition operator for RCS is described by the 2 scalar amplitudes A_1 and A_2 , and 4 spin amplitudes A_3 to A_6 .

Due to the transversality condition $\vec{\epsilon} \cdot \hat{k} = \vec{\epsilon}' \cdot \hat{k}' = 0$, only 2 amplitudes contribute in the forward direction, $\hat{k} = \hat{k}'$, and with some change of notation, $f = A_1$ and $g = A_3$, the forward scattering amplitude reads

$$\mathcal{T}(\omega, \theta = 0) = \hat{\epsilon}'^* \cdot \hat{\epsilon} f(\omega) + i(\hat{\epsilon}'^* \times \hat{\epsilon}) \cdot \vec{\sigma} g(\omega) . \quad (6)$$

II. Virtual Compton Scattering (VCS)

Since this process describes a reaction rather than a scattering, namely the transition from a virtual photon γ^* with $k^2 = -Q^2 < 0$ to a real, massless photon γ , time reversal does not provide any constraint, and all 8 combinations of Eq. (5) are allowed. In addition there are 4 interference terms between the longitudinal helicity of the virtual photon and the transverse helicity of the real photon, which can be found by replacing the transverse polarization vector $\vec{\epsilon}$ in Eq. (5) by the longitudinal polarization vector \hat{k} . The VCS Compton tensor then takes the form

$$\begin{aligned} \mathcal{T}_{VCS} = & \mathcal{T}_{RR} + \vec{\epsilon}'^* \cdot \hat{k} A_9 + i\vec{\sigma} \cdot (\hat{k}' \times \hat{k}) \vec{\epsilon}'^* \cdot \hat{k} A_{10} \\ & + i\vec{\sigma} \cdot (\vec{\epsilon}'^* \times \hat{k}) A_{11} + i\vec{\sigma} \cdot (\vec{\epsilon}'^* \times \hat{k}') A_{12} . \end{aligned} \quad (7)$$

Altogether there appear 3 scalar and 9 spin amplitudes in VCS.

III. Doubly virtual Compton scattering (VVCS)

In comparing with the case of VCS, we find 4 more longitudinal-transverse interference terms by replacing $\vec{\epsilon}'^* \rightarrow \vec{\epsilon}$ and $\hat{k} \rightarrow \hat{k}'$ in the last 4 terms of Eq. (7). Furthermore, there appear 2 terms constructed from the longitudinal-longitudinal combination (Replace $\vec{\epsilon}'^*$ by \hat{k}' in the terms with A_9 and A_{11} of Eq. (7)!). The complete form is

$$\begin{aligned} \mathcal{T}_{VVCS} = & \mathcal{T}_{VCS} + \vec{\epsilon} \cdot \hat{k}' A_{13} + i\vec{\sigma} \cdot (\hat{k} \times \hat{k}') \vec{\epsilon} \cdot \hat{k}' A_{14} + i\vec{\sigma} \cdot (\vec{\epsilon} \times \hat{k}') A_{15} \\ & + i\vec{\sigma} \cdot (\vec{\epsilon} \times \hat{k}) A_{16} + \hat{k} \cdot \hat{k}' A_{17} + i\vec{\sigma} \cdot (\hat{k}' \times \hat{k}) A_{18} . \end{aligned} \quad (8)$$

Up to this point we have considered the general reaction $\gamma^*(Q^2) \rightarrow \gamma^*(Q'^2)$. If we restrict the discussion to photons with equal virtuality in the initial and final states, $Q^2 = Q'^2$, time reversal invariance leads to additional constraints: $A_7 = A_8 = 0$ as for RCS, and the relations $A_9 = A_{13}$, $A_{10} = -A_{14}$, $A_{11} = A_{15}$, $A_{12} = A_{16}$, which leaves 12 independent amplitudes. In the forward direction the amplitude reads

$$\begin{aligned} \mathcal{T}_{VVCS}(\theta = 0) = & \hat{\epsilon}'^* \cdot \hat{\epsilon} f_T(\omega, Q^2) + f_L(\omega, Q^2) + i(\hat{\epsilon}'^* \times \hat{\epsilon}) \cdot \vec{\sigma} g_{TT}(\omega, Q^2) \\ & + i\vec{\sigma} \cdot [(\vec{\epsilon} - \vec{\epsilon}'^*) \times \hat{k}] g_{LT}(\omega, Q^2) , \end{aligned} \quad (9)$$

with $f_T = A_1$, $f_L = A_{17}$, $g_{TT} = A_3$, $g_{LT} = A_{11} + A_{12} + A_{15} + A_{16}$. The 4 amplitudes $\{f_T, f_L, g_{TT}, g_{LT}\}$ can be constructed from the 4 inclusive electroproduction cross sections $\{\sigma_T, \sigma_L, \sigma_{TT}, \sigma_{LT}\}$ by means of forward dispersion relations.

2.1. Real Compton Scattering (RCS)

The forward amplitude for RCS, Eq. (6), can be determined by the double polarization experiment of Fig. 1. The crossing symmetry requires that f is an even and g an odd function of the photon *lab* energy $\nu = E_\gamma$. These amplitudes can be constructed by dispersion relations (DR) based on analyticity (required by causality) and unitarity (the optical theorem in forward direction),

$$\text{Re } f(\nu) = f(0) + \frac{\nu^2}{2\pi^2} \int_{\nu_0}^{\infty} \frac{\sigma_T(\nu')}{\nu'^2 - \nu^2} d\nu' , \quad (10)$$

$$\text{Re } g(\nu) = \frac{\nu}{4\pi^2} \mathcal{P} \int_{\nu_0}^{\infty} \frac{\sigma_{1/2}(\nu') - \sigma_{3/2}(\nu')}{\nu'^2 - \nu^2} \nu' d\nu' . \quad (11)$$

These results may be expanded into a Taylor series for small values of ν and compared to the low energy theorem of Low ⁸, and Gell-Mann and Goldberger ⁹, which expresses the leading term of the amplitudes by the charge e_N and the anomalous magnetic moment κ_N ,

$$f(\nu) = -\frac{e^2 e_N^2}{4\pi M} + (\alpha + \beta) \nu^2 + \mathcal{O}(\nu^4) , \quad (12)$$

$$g(\nu) = -\frac{e^2 \kappa_N^2}{8\pi M^2} \nu + \gamma_0 \nu^3 + \mathcal{O}(\nu^5) . \quad (13)$$

The result of the comparison is Baldin's sum rule ¹⁰,

$$\alpha + \beta = \frac{1}{2\pi^2} \int_{\nu_0}^{\infty} \frac{\sigma_T(\nu')}{\nu'^2} d\nu' , \quad (14)$$

the sum rule of Gerasimov ¹¹, Drell and Hearn ¹²,

$$\frac{\pi e^2 \kappa_N^2}{2M^2} = \int_{\nu_0}^{\infty} \frac{\sigma_{3/2}(\nu') - \sigma_{1/2}(\nu')}{\nu'} d\nu' \equiv I , \quad (15)$$

and the sum rule for the forward spin polarizability ^{9,13},

$$\gamma_0 = -\frac{1}{4\pi^2} \int_{\nu_0}^{\infty} \frac{\sigma_{3/2}(\nu') - \sigma_{1/2}(\nu')}{\nu'^3} d\nu' . \quad (16)$$

Real Compton scattering at general angles requires to set up DR for all 6 amplitudes, i.e., to evaluate the real part of these amplitudes by the

pole term contributions (see graphs a, b, and f of Fig. 2) and integrals over the imaginary part. The latter can be constructed from the respective photoproduction processes, e.g., $\gamma + N \rightarrow \pi + N$ and production of heavier systems like $\pi\pi, \eta$, etc., as described by the SAID or MAID analyses. For

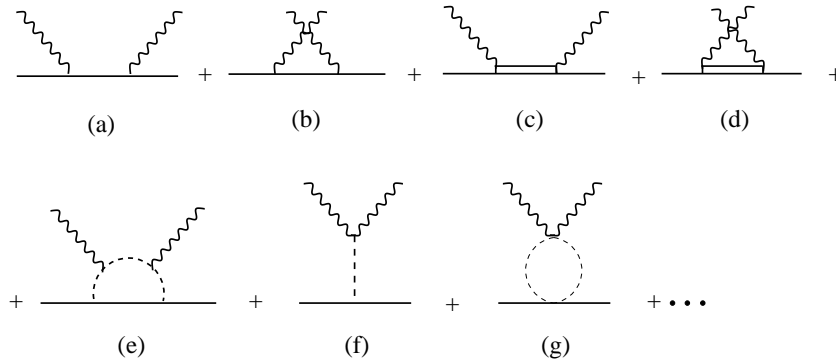


Figure 2. Graphs contributing to Compton scattering off the nucleon. Upper row: The direct (a) and crossed (b) Born diagrams with intermediate nucleons, a typical resonance excitation in the s -channel (c), and its crossed version (d). Lower row: Typical mesonic contributions with photon scattering off an intermediate pion (e), the pion pole diagram (f), and a correlated two-pion exchange such as the “ σ meson” (g).

example, Fig. 2(c) represents a resonance contribution yielding imaginary parts in the s -channel region, (g) leads to imaginary parts in the t -channel region, and the pion-loop diagram (e) may produce imaginary parts in both s and t channel, depending on how one “cuts” the diagram.

Our recent work ¹⁴ includes 4 types of DR: DR at constant t and hyperbolic DR, in both an unsubtracted and a subtracted version, while the previous analysis was essentially based on unsubtracted DR at $t = const.$ The dispersion integrals run over the variable ν , which for general kinematics is defined as the average over the initial and final photon lab energies, $\nu = (E_\gamma + E'_\gamma)/2$, typically up to $E_\gamma \approx 1.5$ GeV. In the case of unsubtracted DR, some of these integrals do not converge, and the contribution from the higher energies is modelled by t -channel poles, in particular the (known) π^0 pole and the exchange of a “ σ meson” with spin and isospin zero. In order to reduce the phenomenology involved with heavier intermediate mass states and the σ meson, we have subtracted such DR at $\nu = 0$. The subtraction function is then constructed by once subtracted dispersion integrals in t , by use of experimental information on the reaction $\gamma + \gamma \rightarrow \pi + \pi$ and an extrapolation of pion-nucleon scattering into the unphysical region ¹⁵. While the subtraction improves the convergence at large ν , it has a shortcoming

at small ν : The dispersion integrals get contributions from outside of the physical region, for which the integrand is constructed by an extension of the partial wave expansion to unphysical angles. This limits the calculation to low partial waves or photon energies below the Δ resonance.

In order to improve the convergence for larger values of t , fixed-angle (or hyperbolic) DR have been proposed¹⁶ and applied to Compton scattering^{17,18}. In particular for $\theta_{\text{lab}} = 180^\circ$, the path of integration runs along the lower boundary of the s -channel region from infinity to the origin of the Mandelstam plane (“ s -channel contribution”), and then continues along a path in the upper half-plane (“ t -channel contribution”). The recent calculations of Pasquini¹⁹ explain, for the first time, the puzzle of the large difference of the electric (α) and magnetic (β) polarizabilities known from backward Compton scattering. For example, the recent experiment with TAPS at MAMI resulted in $(\alpha - \beta)_{\text{exp}} = [10.7 \pm 0.6(\text{stat}) \pm 0.8(\text{syst})]$, here and in the following in units of 10^{-4} fm^3 , while DR at $t = \text{const}$ predict $\alpha - \beta \approx -6$ for the πN intermediate states and an upper limit of integration $E_\gamma = 1.5 \text{ GeV}$. Within the framework of unsubtracted DR at $t = \text{const}$, the discrepancy is then described by heavier intermediate states and the contribution of a σ -meson pole in the t -channel. However, within the framework of hyperbolic DR¹⁹, the result is $(\alpha - \beta)_{\text{hyp}} = 10.9$, obtained by adding the s -channel contribution at $\theta = 180^\circ$, $(\alpha - \beta)_s = -5.6$ and its continuation into the t -channel, $(\alpha - \beta)_t = 16.5$.

Besides the static polarizabilities, it is also possible to define “dynamical” polarizabilities as function of ν , e.g., the dynamical electric dipole polarizability $\alpha_{E1}(\nu)$ with $\alpha_{E1}(0) = \alpha$. This procedure requires a decomposition of the Compton amplitudes into a partial wave series²⁰ of dipole and higher order multipoles including retardation or dispersion effects. The dynamical polarizabilities allow for a very detailed study of the internal degrees of freedom. For example, α_{E1} and α_{E2} clearly show cusp effects at the pion threshold, and β_{M1} exhibits the Δ -resonance structure, with its real part passing through zero at the resonance position. Except for β_{M2} , the HBChPT calculation nicely reproduces the results of DR¹⁹.

2.2. Virtual Compton Scattering (VCS)

The DR formalism has been extended to VCS, a tool to extract generalized polarizabilities (GPs) by means of radiative electron scattering. These GPs are functions of the virtuality of the incident photon and describe, in some sense, the spatial distribution of the polarizabilities. The first unpolarized VCS observables have been obtained from MAMI²¹ at a virtuality $Q^2 = 0.33 \text{ GeV}^2$, and recently at JLab²² at higher virtualities,

$1 \text{ GeV}^2 < Q^2 < 2 \text{ GeV}^2$. Further experimental programs are underway at the intermediate energy electron accelerators (MIT-Bates ²³, MAMI ²⁴, and JLab ²⁵) to measure both unpolarized and polarized VCS observables. The existing data indicate a Q^2 dependence of the electric GP similar to a dipole form factor, whereas the magnetic GP follows a more complicated Q^2 behavior. As was already shown for RCS, the magnetic dipole transition involves a strong cancellation between the diamagnetism due to the pion cloud effects (essentially the “asymptotic” or t-channel contribution) and the paramagnetism due to resonance excitation (essentially the quark spin-flip transition to the Δ resonance in the s-channel). Since the cloud effects have a considerably longer range in space than the resonance structures, the Q^2 behavior of the magnetic GP is able to disentangle both physical mechanisms, which is already displayed in the existing data. Given this initial success, future experiments to measure VCS observables in the Δ region hold the promise to extract GPs with an enhanced precision, within the DR formalism.

2.3. *Doubly Virtual Compton Scattering*

As has been shown in Eq. (9), forward VVCS is described by 4 independent amplitudes, which can be constructed from the partial cross sections of Eq. (2). In this sense the sum rules of Eqs. (14) to (16) may be generalized to virtual photons ^{14,26}, and 2 further sum rules can be constructed for the amplitudes f_L and g_{LT} involving the longitudinal photon. In particular the “generalized GDH integral” $I(Q^2)$ was recently measured at the Jefferson Lab ²⁷ for both the proton and the neutron. These data indicate a dramatic “phase transition” between the resonance dominated region at $Q^2 \lesssim 1 \text{ GeV}^2$ and the regime of DIS at the larger values of Q^2 , in qualitative agreement with the results of DR at low Q^2 and perturbative QCD at large Q^2 ²⁸.

Due to the weighting with the energy denominators, the generalized forward spin polarizability $\gamma_0(Q^2)$ and the longitudinal-transverse polarizability $\delta_{LT}(Q^2)$, related to the amplitudes g_{TT} and g_{LT} of Eq. (9), respectively, are determined by resonance and pionic degrees of freedom. The observable $\gamma_0(Q^2)$ was recently determined at $Q^2 = 0$ by the GDH experiment at MAMI. The small value $\gamma_0(0) \approx [-1.01 \pm 0.08(\text{stat}) \pm 0.10(\text{syst})] \cdot 10^{-4} \text{ fm}^4$ is well reproduced by a strong cancellation of S-wave pion production and Δ excitation in DR ²⁹, while the existing results of ChPT scatter around this value. The ChPT prediction ³⁰ at $\mathcal{O}(p^4)$, on the other hand, agrees quite well with the result of DR, $\delta_{LT}(0) \approx 1.4 \cdot 10^{-4} \text{ fm}^4$. However, practically nothing is known so far about $\delta_{LT}(Q^2)$ from the experimental side. It

will be interesting to study the Q^2 dependence of these VVCS observables in more detail, both theoretically and experimentally.

References

1. D. Babusci, G. Giordano, and G. Matone, *Phys. Rev.* **C57**, 291 (1998).
2. S. Chekanov *et al.* (ZEUS Collaboration), *Nucl. Phys.* **B627**, 3 (2002).
3. J. Ahrens *et al.* (GDH and A2 Coll.), *Phys. Rev. Lett.* **84**, 5950 (2000).
4. K. Helbing (GDH Collaboration), *Nucl. Phys.(Proc. Suppl.)* **B105**, 113 (2002); P. Grabmayr, *these proceedings*.
5. D. Drechsel, S.S. Kamalov, and L. Tiator, *Phys. Rev.* **D63**, 114010 (2001).
6. A. L'vov, V. A.Petrun'kin, and M. Schumacher, *Phys. Rev.* **C55**, 359 (1997).
7. T.R. Hemmert, B. R. Holstein, J. Kambor, and G. Knöchlein, *Phys. Rev.* **D57**, 5746 (1998).
8. F.E. Low, *Phys. Rev.* **96**, 1428 (1954).
9. M. Gell-Mann and M.L. Goldberger, *Phys. Rev.* **96**, 1433 (1954).
10. A.M. Baldin, *Nucl. Phys.* **18**, 310 (1960).
11. S. Gerasimov, *Yad. Fiz* **2**, 598 (1965) [*Sov. J. Nucl. Phys.* **2**, 430 (1966)].
12. S. D. Drell and A. C. Hearn, *Phys. Rev. Lett.* **16**, 908 (1966).
13. M. Gell-Mann, M.L. Goldberger, and W.E. Thirring, *Phys. Rev.* **95**, 1612 (1954).
14. D. Drechsel, B. Pasquini, and M. Vanderhaeghen, *Dispersion relations in real and virtual Compton scattering*, to be published.
15. D. Drechsel, M. Gorchtein, B. Pasquini, and M. Vanderhaeghen, *Phys. Rev.* **C61**, 015204 (1999).
16. J. Bernabeu, T. E. O. Ericson, and C. Ferro Fontan, *Phys. Lett.* **49B**, 381 (1974); J. Bernabeu and B. Tarrach, *ibid.* **69B**, 484 (1977).
17. B.R. Holstein and A.M. Nathan, *Phys. Rev.* **D49**, 6101 (1994).
18. A.I. L'vov and A.M. Nathan, *Phys. Rev.* **C59**, 1064 (1999).
19. B. Pasquini, *these proceedings*.
20. D. Babusci, C. Giordano, A. I. L'vov, G. Matone, and A. M. Nathan, *Phys. Rev. C* **58**, 1013 (1998).
21. J. Roche *et al.*, *Phys. Rev. Lett.* **85**, 708 (2000).
22. H. Fonvieille (Jefferson Lab Hall A and VCS Collaborations), hep-ex/0206035.
23. R. Miskimen, spokesperson MIT-Bates experiment, 97-03.
24. N. d'Hose and H. Merkel, spokespersons MAMI experiment (2001).
25. C. Hyde-Wright, G. Laveissière, private communication.
26. T.R. Hemmert, *these proceedings*.
27. K. de Jager, *these proceedings*, and references given therein.
28. M. Anselmino, *these proceedings*; S. Simula, *these proceedings*.
29. L. Tiator, *these proceedings*.
30. C.W. Kao, *these proceedings*.